Journal of Sound and Vibration 630 (2026) 119700

Contents lists available at ScienceDirect

Journal of Sound and Vibration

journal homepage: www.elsevier.com/locate/jsvi

Mode conversion for elastic waves via anisotropic temporal interfaces

Cong Chen [a], Zhanyu Li [a], Xiaoming Zhou [a,*], Gengkai Hu [b,*]

[a] School of Aerospace Engineering, Beijing Institute of Technology, Beijing 100081, China
[b] Marine Science and Technology Domain, Beijing Institute of Technology (Zhuhai), Zhuhai 519088, China

ARTICLE INFO

Keywords:
Mode conversion
Temporal interface
Elastic waves
Anisotropy
Time-varying modulation

ABSTRACT

Customizing elastic wave polarization is a challenging task due to the complex interactions between waves and solids. In this work, perfect mode conversion from longitudinal to transverse waves is achieved by employing an isotropic-anisotropic-isotropic temporal interface. A general transfer matrix method is developed based on the continuity conditions at temporal interfaces, enabling the analysis of elastic wave propagation in temporally layered orthotropic structures. This method provides the calculations of transmission and reflection coefficients for both longitudinal and transverse polarization modes. Within this framework, a general route to complete elastic wave mode conversion is proposed and validated through finite-difference time-domain simulations. Furthermore, the underlying physical mechanism is elucidated through polarization trajectory analysis. This research provides a new approach for elastic wave control through time-varying materials.

Introduction

The polarization of elastic waves characterizes the vibration direction of material particles with respect to the wave propagation direction [1]. Efficient mode conversion for elastic waves remains a challenging task due to their strong mode couplings. Among them, the mode conversion from the longitudinal (P) to shear (S) wave mode has attracted lots of attention since it holds great promise for applications in non-destructive evaluation of structures [2–4], ultrasonic elastography [5] and medical diagnosis [6]. In the past decade, the emergence of elastic metamaterials (EMMs) has provided a powerful method for the elastic wave control [7–10]. Different methods have been put forward to achieve elastic wave conversion based on EMMs. As examples, mode conversion between P and S waves can be facilitated via a double-negative EMM [7,11]. Transmodal Fabry-Perot resonance (TFPR) is also utilized to achieve mode conversion when the thickness of the anisotropic elastic metamaterial layer is an integer multiple of half-wavelength under low-reflectivity and weak coupling conditions [12]. This advancement further leads to the proposal of the conditions for near-perfect mode conversion through TFPR [13]. Besides, nearly full mode-converting transmissions can be realized using bimodal quarter-wave impedance-matching theory [14] and validated by a single-phase “monolayer” anisotropic metamaterial [15]. Most EMM-based methods reported so far make use of the complex spatial modulation of materials properties, and the complete mode conversion remains still difficult to achieve.

Recently, time-varying or temporal metamaterials, allowing time modulation of material properties, unlock a new degree of

---

* Corresponding authors.
E-mail addresses: zhxming@bit.edu.cn (X. Zhou), hugeng@bit.edu.cn (G. Hu).

https://doi.org/10.1016/j.jsv.2026.119700
Received 2 June 2025; Received in revised form 9 January 2026; Accepted 5 February 2026

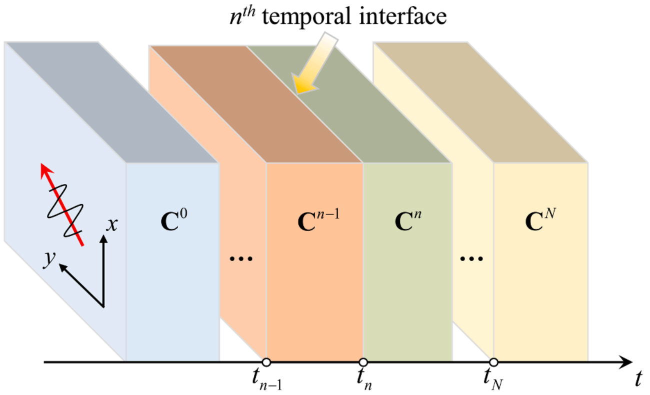

Fig. 1. Schematic of theoretical model of elastic wave scatterings by temporal interfaces, where a homogeneous elastic medium with the elasticity tensor $\mathbf{C}^0$ is suddenly changed to the medium with $\mathbf{C}^n$ at time t_n.

freedom for wave manipulation. The concept of "time-varying media" originated in the fields of electromagnetics and optics [16,17], enabling functionalities that are not achievable with time-invariant systems, such as nonreciprocal propagation [18], spatiotemporal modulation [19] and time reversal [20]. In recent years, this concept has been extended to the realm of elastic waves [21,22] with an interest on periodic temporal modulation or spatiotemporal modulation. Time modulation of material properties, typically including modulated mass [23] and stiffness [24], can support nonreciprocal wave propagation by breaking time reversal symmetry [25,26], which has been realized in space-time metamaterial beam [27,28]. The transmission and reflection at a single moving interface, which forms the fundamental unit of space-time modulation, have also been extensively studied [29], and experimentally verified [30]. Studies also demonstrated the linkage between space-time modulated materials and Willis dynamic materials [31–33]. Temporal metamaterials have opened a new route for elastic wave tailoring, such as bandgap control [25,34], energy accumulation [35], field patterns [36,37], mode conversion [38,39], wave guiding [40], and unidirectional wave propagation [41].

A distinctive type of time-varying media, known as “temporal interface”, features an abrupt change in material parameters over time while maintaining spatial uniformity. It is the temporal analog of the well-known spatial interface between two different media. This concept has recently attracted growing attention due to its potential for creating novel wave behaviors [42–44], such as the inverse prism [45], antireflection temporal coatings [46], and temporal Fabry-Perot slab [47]. Initial research primarily focuses on isotropic-isotropic temporal interfaces, which are analogous to spatial interfaces between two semi-infinite media under normal incidence. When anisotropic temporal interfaces are introduced, a broader range of wave phenomena and functionalities can emerge, such as polarization conversion [48], temporal aiming [49] and temporal equivalent of Brewster angle [50]. While temporal interfaces demand a modulation rate significantly exceeding the wave frequency, which is rather challenging, successful experimental realizations have been reported in a few cases involving electromagnetic waves [51], water waves [20], acoustic waves [52], and even elastic waves [53].

Nearly all studies of temporal interfaces focus on electromagnetic waves, with limited exploration in the context of elastic wave control. This paper will extend the concept of temporal interfaces to elastic waves, and the characteristics of temporal interfaces for elastic waves will be examined to demonstrate its ability to facilitate perfect mode conversion. The fundamental concepts and properties of anisotropic temporal interfaces for elastic waves will be studied in Section 2. A temporal transfer matrix method for a general elastic medium will be presented to analyze the wave scattering problem for multi-layered temporal structure. In Section 3, we will analyze the condition of perfect mode conversion in an isotropic-anisotropic-isotropic temporal structure, and reveal the physical mechanism of temporal interfaces for achieving complete mode conversion. In Section 4, a Finite-Difference Time-Domain (FDTD) method will be developed to validate the theoretical findings for perfect conversion from P to S waves. The dynamic behavior of the particle trajectory and energy flux associated with the temporal interface will be also discussed. Finally, conclusions are drawn in Section 5.

Elastic wave scatterings by temporal interfaces

Consider an infinite and spatially homogeneous two-dimensional (2D) elastic medium in the plane-strain state with a constant mass density ρ. The elasticity of the medium varies in time: the elasticity tensor initially takes the value $\mathbf{C}^0$, undergoes instantaneous changes to $\mathbf{C}^n$ at an instant t_n $(1 \le n \le N)$, and ultimately reaches $\mathbf{C}^N$ after t_N. Without loss of generality, the initial and end media are assumed to be isotropic in elasticity, while each temporal layer $(t_n \le t \le t_{n+1})$ is of anisotropic elasticity. At time $t < t_1$, a plane longitudinal wave with frequency ω_0 and wave vector $\mathbf{k}$ propagates in the direction at an angle α from the x axis, as illustrated in Fig. 1. In the nth temporal region, the elastodynamic equation is given by

$$\frac{\mathrm{d}\mathbf{p}}{\mathrm{d}t} = \nabla \cdot \left[\mathbf{C}^n : (\nabla \mathbf{u} + \mathbf{u}\nabla) / 2\right] \tag{1}$$

where $\mathbf{p} = \rho d\mathbf{u}/dt$ is the momentum density, and $\mathbf{u} = \left[u_x, u_y\right]^{\mathrm{T}}$ is the displacement vector. In the following studies, we will formulate the solutions for elastic wave scattering at multilayered anisotropy temporal interfaces, and investigate the mode conversion between differently polarized elastic waves.

A 2D elastic medium allows two polarization states of elastic waves, where both forward and backward propagating modes are supported for each polarized state. Therefore, there exist four types of waves in each temporal layer. The displacement field $\mathbf{u}^n$ in the n^{th} temporal layer can be expressed as a linear superposition of four scattered waves

$$\mathbf{u}^n = \sum_{m=1}^{4} A_m^n \mathbf{u}_m^n e^{i\left(\omega_m^n (t-t_n) - \mathbf{k}_m^n \cdot \mathbf{r}\right)} \tag{2}$$

where A_m^n and $\mathbf{u}_m^n$ represent the wave amplitude and unit polarization state vector of the mth type of waves. $\boldsymbol{k}_m^n$ and ω_m^n are corresponding wave vectors and frequencies, respectively.

The intrinsic understanding of temporal interfaces is crucial to the formulation of elastic wave solutions. Take the temporal interface at t_n as an example, across which the elasticity tensor is suddenly changed from $\mathbf{C}^{n-1}$ to $\mathbf{C}^n$. Choose an infinitesimal time interval ε, and integrate Eq. (1) from t_n^- to t_n^+, where $t_n^{\pm} = t_n \pm \varepsilon/2$. In the limit of $\varepsilon \to 0$, it can be derived that the particle displacement and momentum are conserved at the temporal interface as given by

$$\mathbf{u}|_{t=t_n^-} = \mathbf{u}|_{t=t_n^+}, \quad \mathbf{p}|_{t=t_n^-} = \mathbf{p}|_{t=t_n^+} \tag{3}$$

The conservation of particle momentum across a temporal interface is a result of spatial translation symmetry [54], which holds true for a general time-varying medium.

Substitution of Eq. (2) into Eq. (3) gives rise to

$$\sum_{m=1}^{4} A_m^n \begin{pmatrix} \mathbf{u}_m^n \\ \mathbf{v}_m^n \end{pmatrix} e^{-i\left(\mathbf{k}_m^n \cdot \mathbf{r} - \omega_m^n (t-t_n)\right)} \Bigg|_{t=t_n^+} = \sum_{m=1}^{4} A_m^{n-1} \begin{pmatrix} \mathbf{u}_m^{n-1} \\ \mathbf{v}_m^{n-1} \end{pmatrix} e^{-i\left(\mathbf{k}_m^{n-1} \cdot \mathbf{r} - \omega_m^{n-1} (t-t_{n-1})\right)} \Bigg|_{t=t_n^-} \tag{4}$$

where $\mathbf{v}_{\mathrm{m}}^{\mathrm{n}}$ refers to the velocity vector, and the time-invariance of mass density has been used. Notice that the local time $(t - t_n)$ in the n^{th} layer is defined such that the phase evolution within each time layer starts with zero, and will simplify the analytic expression. Alternatively, the global time t can also be used, and will lead to the same results. Since Eq. (4) holds for arbitrary points in space, we can derive the continuity condition of wave vectors, namely $\mathbf{k}_m^n = \mathbf{k}_m^{n-1} \equiv \mathbf{k}$. Due to the conservation of $\mathbf{k}$, waves with different polarization states have different frequencies, as will be discussed in detail in Section 3.

Eq. (4) can be rearranged as the following expressions

$$\begin{cases} \sum_{m=1}^{4} A_m^{n-1} \mathbf{u}_m^{n-1} \cdot \hat{\mathbf{x}} e^{i\omega_m^{n-1}\tau_{n-1}} = \sum_{m=1}^{4} A_m^n \mathbf{u}_m^n \cdot \hat{\mathbf{x}} \\ \sum_{m=1}^{4} A_m^{n-1} \mathbf{u}_m^{n-1} \cdot \hat{\mathbf{y}} e^{i\omega_m^{n-1}\tau_{n-1}} = \sum_{m=1}^{4} A_m^n \mathbf{u}_m^n \cdot \hat{\mathbf{y}} \\ \sum_{m=1}^{4} A_m^{n-1} \mathbf{v}_m^{n-1} \cdot \hat{\mathbf{x}} e^{i\omega_m^{n-1}\tau_{n-1}} = \sum_{m=1}^{4} A_m^n \mathbf{v}_m^n \cdot \hat{\mathbf{x}} \\ \sum_{m=1}^{4} A_m^{n-1} \mathbf{v}_m^{n-1} \cdot \hat{\mathbf{y}} e^{i\omega_m^{n-1}\tau_{n-1}} = \sum_{m=1}^{4} A_m^n \mathbf{v}_m^n \cdot \hat{\mathbf{y}} \end{cases} \tag{5}$$

where $\hat{\mathbf{x}}$ and $\hat{\mathbf{y}}$ denote unit vectors along x and y directions, and τ_n is the time duration of the n^{th} temporal layer. Eq. (5) can be further expressed in matrix notation as

$$\mathbf{D}_{n-1}\mathbf{P}_{n-1}\mathbf{A}_{n-1} = \mathbf{D}_n \mathbf{A}_n \tag{6}$$

where $\mathbf{A}_n = \left[A_1^n, A_2^n, A_3^n, A_4^n\right]^{\mathrm{T}}$, $\mathbf{P}_n$ follows

$$\mathbf{P}_n = \begin{cases} \mathrm{diag}\left(e^{i\omega_0 t_1}, e^{i\omega_0 t_1}, e^{i\omega_0 t_1}, e^{i\omega_0 t_1}\right), & n = 0 \\ \mathrm{diag}\left(e^{i\omega_1^n \tau_n}, e^{i\omega_2^n \tau_n}, e^{i\omega_3^n \tau_n}, e^{i\omega_4^n \tau_n}\right), & n \geq 1 \end{cases} \tag{7}$$

and $\mathbf{D}_n$ is given by

$$\mathbf{D}_n = \begin{bmatrix} \mathbf{u}_1^n \cdot \hat{\mathbf{x}} & \mathbf{u}_2^n \cdot \hat{\mathbf{x}} & \mathbf{u}_3^n \cdot \hat{\mathbf{x}} & \mathbf{u}_4^n \cdot \hat{\mathbf{x}} \\ \mathbf{u}_1^n \cdot \hat{\mathbf{y}} & \mathbf{u}_2^n \cdot \hat{\mathbf{y}} & \mathbf{u}_3^n \cdot \hat{\mathbf{y}} & \mathbf{u}_4^n \cdot \hat{\mathbf{y}} \\ \mathbf{v}_1^n \cdot \hat{\mathbf{x}} & \mathbf{v}_2^n \cdot \hat{\mathbf{x}} & \mathbf{v}_3^n \cdot \hat{\mathbf{x}} & \mathbf{v}_4^n \cdot \hat{\mathbf{x}} \\ \mathbf{v}_1^n \cdot \hat{\mathbf{y}} & \mathbf{v}_2^n \cdot \hat{\mathbf{y}} & \mathbf{v}_3^n \cdot \hat{\mathbf{y}} & \mathbf{v}_4^n \cdot \hat{\mathbf{y}} \end{bmatrix} \tag{8}$$

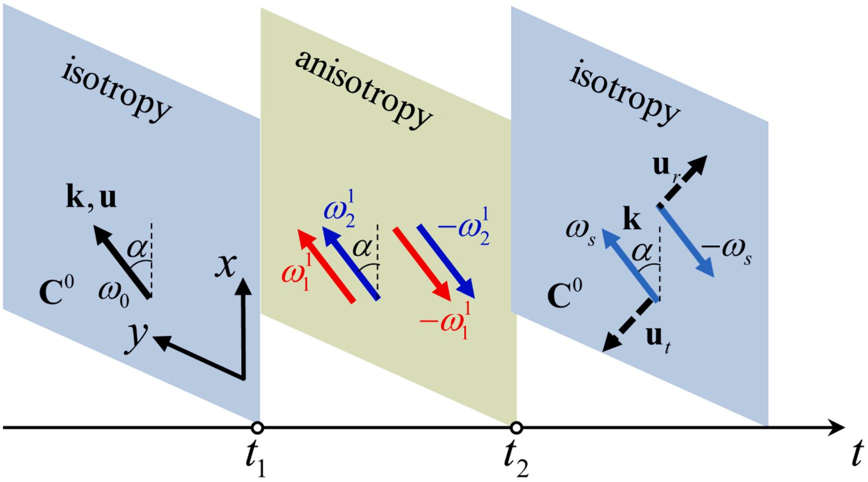

Fig. 2. Schematic of mode conversion through the 1-2-1 temporal structure. Along the time axis from left to right are initial (isotropic), middle (anisotropic) and end (isotropic) layers, respectively. The directions of solid arrows indicate the direction of wave propagation, while different colors represent waves of different frequencies. Arrows aligned with or opposite to the wavevector $\mathbf{k}$ indicate waves with positive or negative frequencies. $\mathbf{u}_t$ and $\mathbf{u}_r$ represent the displacement vectors of the transmitted and reflected waves in the end layer, which are perpendicular to $\mathbf{k}$.

where $\mathbf{u}_1^n = \mathbf{u}_3^n, \mathbf{u}_2^n = \mathbf{u}_4^n$ correspond to the longitudinal and transverse polarization states respectively, and $\mathbf{v}_m^n = i\omega_m^n \mathbf{u}_m^n$. Consider a plane longitudinal wave with incident angle α that travels in the isotropic medium, as shown in Fig. 1. The eigenvectors in the initial and end layers are $\mathbf{u}_1^0 = \mathbf{u}_1^N = [\cos\alpha, \sin\alpha]^{\mathrm{T}}, \mathbf{u}_2^0 = \mathbf{u}_2^N = [\sin\alpha, -\cos\alpha]^{\mathrm{T}}$.

According to Eq. (6), the relationship of wave amplitudes between the initial and end layers can be derived as

$$\mathbf{A}_N = \mathbf{M}\mathbf{A}_0, \mathbf{M} = \left(\mathbf{D}_N^{-1}\mathbf{D}_{N-1}\mathbf{P}_{N-1}\right)\left(\mathbf{D}_{N-1}^{-1}\mathbf{D}_{N-2}\mathbf{P}_{N-2}\right)\cdots\left(\mathbf{D}_1^{-1}\mathbf{D}_0\mathbf{P}_0\right) \tag{9}$$

In the end layer, denote the wave amplitudes of transmitted and reflected longitudinal waves by A_1^N and A_3^N, respectively, and those of transverse waves by A_2^N and A_4^N. According to Eq. (9), the corresponding transmission and reflection coefficients can be derived as

$$\begin{cases} t_p = \dfrac{A_1^N}{A_1^0} = M_{11}, & t_s = \dfrac{A_2^N}{A_1^0} = M_{21} \\ r_p = \dfrac{A_3^N}{A_1^0} = M_{31}, & r_s = \dfrac{A_4^N}{A_1^0} = M_{41} \end{cases} \tag{10}$$

where $M_{ij} = [\mathbf{M}]_{ij}$, and A_1^0 refers to the wave amplitude of the incident longitudinal wave. The temporal transfer matrix method (TTMM) stated above is general, and can be applied to the scenarios where the temporal layers involve sudden changes of both density and elasticity properties, as illustrated in Appendix A.

Wave mode conversion by a temporal orthotropic layer

Based on the three-layer system ($N = 2$) as shown in Fig. 2, the mode conversion between longitudinal and transverse waves by a temporal layer with the orthotropic elasticity will be analyzed in this section. Without loss of generality, the principal axes of the orthotropic medium are set in align with coordinates (x,y), and the corresponding elasticity tensor is given by

$$\mathbf{C}^1 = \begin{bmatrix} C_{11} & C_{12} & 0 \\ C_{12} & C_{22} & 0 \\ 0 & 0 & C_{66} \end{bmatrix} \tag{11}$$

According to the TTMM, the transfer matrix $\mathbf{M}$ in Eq. (9) is given by

$$\mathbf{M} = \mathbf{D}_2^{-1}\mathbf{D}_1\mathbf{P}_1\mathbf{D}_1^{-1}\mathbf{D}_0\mathbf{P}_0 \tag{12}$$

The matrices $\mathbf{P}_0$ and $\mathbf{D}_0$ associated to the incident layer can be determined by Eqs. (7) and (8). The matrix $\mathbf{D}_1$ is related to the polarization state vector $\mathbf{u}_{1,2}^1$ and the frequency ω_m^1 of the orthotropic layer, and can be solved by Eq. (8) ($m = 1 \sim 4$). The direction of wave vector in the orthotropic layer is same to that of the incident wave. Then the eigenvectors $\mathbf{u}_{1,2}^1$ can be derived as the following expression based on Eqs. (1) and (11)

$$\mathbf{u}_{1,2}^{1}=\frac{1}{L}\left[2A_{12},-A+B\pm\sqrt{A^{2}-2AB+B^{2}+4A_{12}^{2}}\right]^{\mathrm{T}} \tag{13}$$

where $L=\sqrt{4A_{12}^{2}+\left(-A+B\pm\sqrt{A^{2}-2AB+B^{2}+4A_{12}^{2}}\right)^{2}}$. The corresponding eigenvalues, namely wave velocities, are given by

$$c_{1,2}^{2}=\frac{(A+B)\pm\sqrt{(A-B)^{2}+4A_{12}^{2}}}{2\rho}\cos^{2}\alpha \tag{14}$$

where

$$A=C_{11}+C_{66}\tan^{2}\alpha,\quad B=C_{22}\tan^{2}\alpha+C_{66},\quad A_{12}=C_{12}\tan\alpha+C_{66}\tan\alpha \tag{15}$$

According to the conservation of the wave vector, the wave frequency ω_{m}^{1} can be determined by the following relation

$$\omega_{1}^{1}=-\omega_{3}^{1}=\frac{|c_{1}|}{|c_{0}|}\omega_{0},\quad \omega_{2}^{1}=-\omega_{4}^{1}=\frac{|c_{2}|}{|c_{0}|}\omega_{0} \tag{16}$$

where c_0 is the velocity of the incident P wave. Eq. (16) can be interpreted as the temporal Snell's law, and the frequency conversion occurs as a consequence of the breaking of the time-translation symmetry [54]. Based on Eqs. (8) and (16), the matrices $\mathbf{P}_1$ and $\mathbf{D}_1$ can be determined.

Four wave modes in the middle layer consist of two quasi-longitudinal (qP) waves and two quasi-shear (qS) waves. For simplicity, we denote the frequencies of these two waves by ω_{qp} and ω_{qs}, which satisfy $\omega_{qp}=\omega_{1}^{1}=-\omega_{3}^{1}$ and $\omega_{qs}=\omega_{2}^{1}=-\omega_{4}^{1}$. The frequencies of P and S waves in the initial and end layer are denoted by $\omega_{p}=\omega_{0}c_{p}/c_{0}=\omega_{0}$ and $\omega_{s}=\omega_{0}c_{s}/c_{0}$, where c_p and c_s are the velocities of the P and S waves in the isotropic medium, respectively. According to Eq. (8), $\mathbf{D}_2$ can be calculated by

$$\mathbf{D}_{2}=\begin{bmatrix}\cos\alpha & \sin\alpha & \cos\alpha & \sin\alpha\\ \sin\alpha & -\cos\alpha & \sin\alpha & -\cos\alpha\\ i\omega_{p}\cos\alpha & i\omega_{s}\sin\alpha & -i\omega_{p}\cos\alpha & -i\omega_{s}\sin\alpha\\ i\omega_{p}\sin\alpha & -i\omega_{s}\cos\alpha & -i\omega_{p}\sin\alpha & i\omega_{s}\cos\alpha\end{bmatrix} \tag{17}$$

Finally, the transmission and reflection coefficients can be computed from Eq. (10).

Complete mode conversion from P wave to S wave occurs when $t_p=r_p=0$, which results in

$$\mathbf{S}\begin{bmatrix}\sin\beta_{\mathbf{qs}}\\ \sin\beta_{\mathbf{qp}}\end{bmatrix}=\mathbf{0},\quad \mathbf{S}=\begin{bmatrix}\mathbf{S}_{1}^{-}(\mathbf{1}-\mathrm{Q}_{1}) & \mathbf{P}_{1}^{-}(\mathbf{1}+\mathrm{Q}_{1})\\ \mathbf{S}_{1}^{+}(\mathbf{1}-\mathrm{Q}_{1}) & \mathbf{P}_{1}^{+}(\mathbf{1}+\mathrm{Q}_{1})\end{bmatrix} \tag{18}$$

and

$$Q_{1}\left(\cos\beta_{qp}-\cos\beta_{qs}\right)+\left(\cos\beta_{qp}+\cos\beta_{qs}\right)=0 \tag{19}$$

where $\beta_{qp}=\omega_{qp}\tau^{1},\beta_{qs}=\omega_{qs}\tau^{1}$ and

$$\begin{cases}Q_{1}=\dfrac{2A_{12}\sin(2\alpha)+\cos(2\alpha)(A-B)}{\sqrt{A^{2}-2AB+4A_{12}{}^{2}+B^{2}}}\\ S_{1}^{-}=\dfrac{\omega_{qs}}{\omega_{0}}-\dfrac{\omega_{0}}{\omega_{qs}},S_{1}^{+}=\dfrac{\omega_{qs}}{\omega_{0}}+\dfrac{\omega_{0}}{\omega_{qs}}\\ P_{1}^{-}=\dfrac{\omega_{qp}}{\omega_{0}}-\dfrac{\omega_{0}}{\omega_{qp}},P_{1}^{+}=\dfrac{\omega_{qp}}{\omega_{0}}+\dfrac{\omega_{0}}{\omega_{qp}}\end{cases} \tag{20}$$

It can be verified that det $(\mathbf{S})\neq 0$. Thus from Eq. (18), we have

$$\sin\beta_{qp}=\sin\beta_{qs}=0 \tag{21}$$

By substituting Eq. (21) into Eq. (19), we can obtain

$$\cos\beta_{qp}=-\cos\beta_{qs} \tag{22}$$

and

$$2A_{12}\sin(2\alpha)+\cos(2\alpha)(A-B)=0 \tag{23}$$

Eqs. (21)-(23) give the conditions for complete mode conversion from P to S wave modes. It is readily found that there is no solution in the case of $\alpha=0^{\circ}$ and 90°, meaning that complete mode conversion cannot be achieved when the incident angle is parallel to the principal axis.

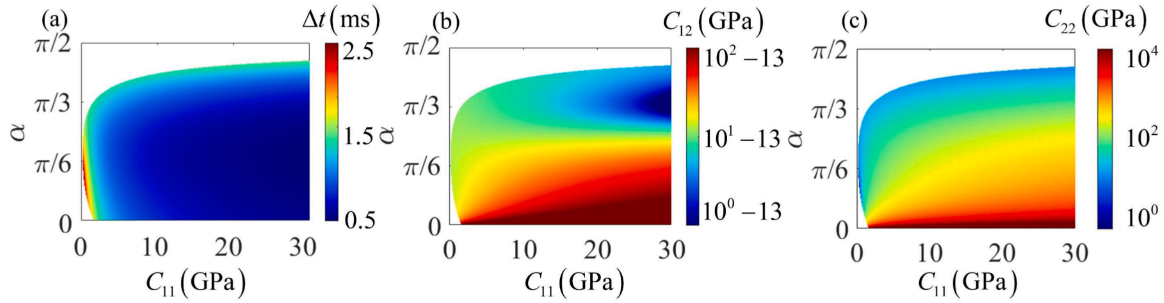

Fig. 3. Results of (a) Δt, (b) C_{12} and (c) C_{22} for the appearance of complete mode conversion upon the variation of α and C_{11}.

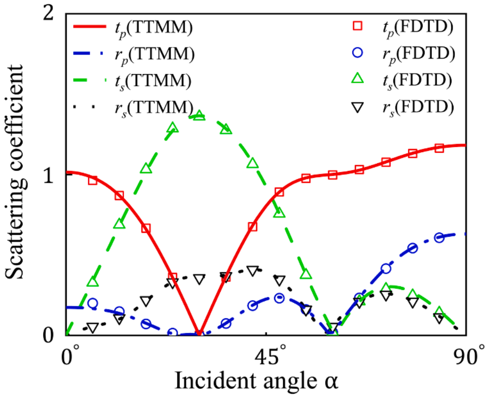

Fig. 4. Comparison of TTMM and FDTD results for $t_p,\ r_p,\ t_s,\ r_s$ as functions of incident angle for system parameters of $C_{12} = 0.5$ GPa, $C_{22} = 10.160$ GPa and $\Delta t = 1.861$ ms.

As examples, consider material parameters $\lambda = 1$ GPa and $\mu = 1$ GPa and $\rho = 10^3$ kg/m^3 for the initial and end layers, and $C_{66} = 1$ GPa for the middle layer. These material parameters are chosen mainly for mathematical convenience and can be physically realized in artificial structured materials as discussed in Sec. 4.3. The frequency of the incident P wave is taken as $f = 0.5$ kHz. The system parameters involve elastic constants C_{11}, C_{12}, C_{22}, the incident angle α and the time duration Δt. Without loss of generality, a set of solutions for Eqs. (21) and (22) are chosen as $\beta_{qp} = 2\pi$ and $\beta_{qs} = \pi$. Only two system parameters are independent when the perfect mode conversion condition is satisfied. Fig. 3 (a-c) show the results of Δt, C_{12} and C_{22} for the appearance of complete mode conversion upon the variation of α and C_{11}. The conditions of $C_{11} > 0$, $C_{22} > 0$ and $C_{11}C_{22} > C_{12}^2$ are required to ensure the positive definiteness of the elastic stiffness matrix **C**. The incident angle α is seen to play a crucial role for the formation of complete mode conversion. Mode conversion hardly occurs when the wave propagation direction is close to the principal axes of the orthotropic medium because the elastic constants C_{12} and C_{22} tend to infinity, or is forbidden by the positive definiteness of **C**.

Results and discussions

In this section, numerical results are presented to verify the theoretical predictions for temporal scattering and mode conversion behavior. The physical mechanism underlying mode conversion is provided, and the evolution of polarization trajectories and energy flux will be discussed.

Scattering analysis for complete mode conversion

Consider system parameters $\alpha = \pi/6$ and $C_{12} = 0.5$ GPa. According to Eqs. (21)-(23), it can be determined that $\Delta t = 1.861$ ms, $C_{11} = 1.053$ GPa and $C_{22} = 10.160$ GPa for the appearance of perfect mode conversion. Based on the TTMM method, the scattering coefficients $t_p,\ r_p, t_s, r_s$ against the variation of incident angles are calculated as shown in Fig. 4, where $C_{12} = 0.5$ GPa is chosen. It is seen that the complete mode conversion with $t_p = 0$ and $r_p = 0$ occurs at $\alpha = \pi/6$, in accordance with the prediction. In this case, the energy is flowed to the S-polarized mode, and dominated by the forward traveling wave.

Physical insights into complete mode conversion can be gained by analyzing the polarization trajectories of particles upon the sudden change of material properties. Consider a plane longitudinal wave propagating with the incident angle $\alpha = \pi/6$. In the initial

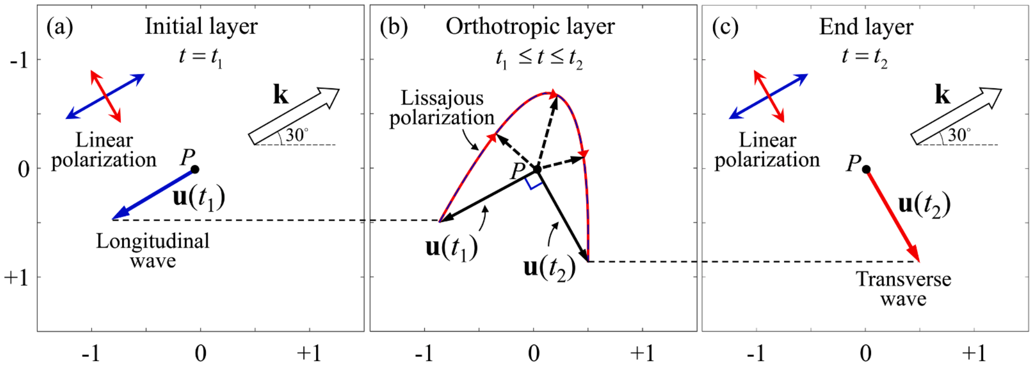

Fig. 5. The particle polarization trajectories in the regime of (a) $t \le t_1^-$, (b) $t_1^+ \le t \le t_2^-$ and (c) $t \ge t_2^+$.

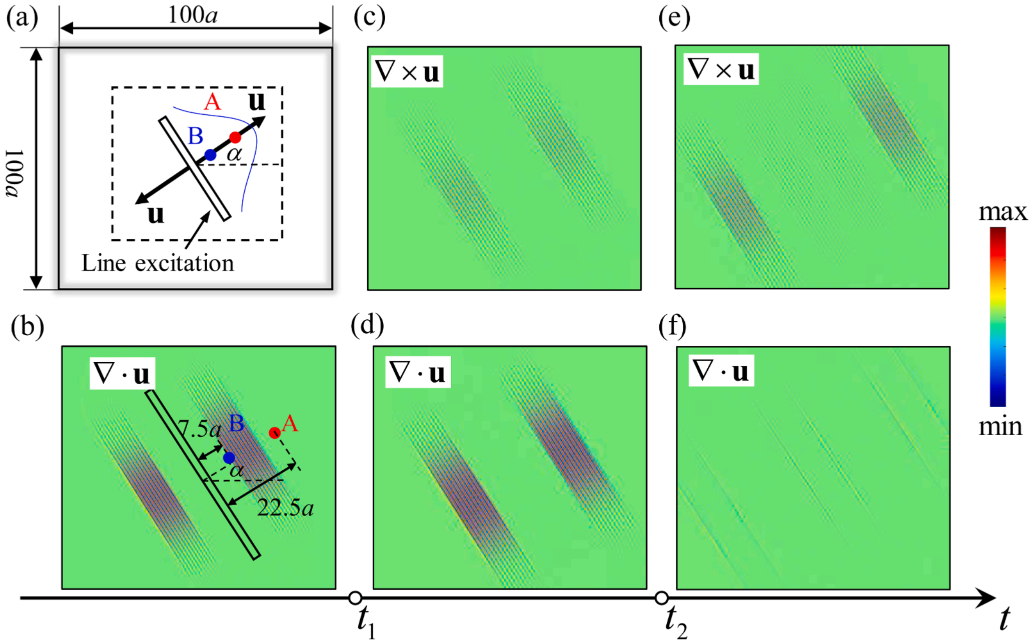

Fig. 6. FDTD results of wave propagation in the isotropic-anisotropic-isotropic temporal slab: (a) the simulation model for FDTD computation; (b) The divergence component of displacement fields at t_1=40 ms; The curl and divergence components of displacement fields at (c,d) 40.93 ms and (e, f) 60 ms.

isotropic medium, the displacement vector for a material point P is in align with the propagation direction $\mathbf{k}$ due to the longitudinal polarization, as sketched in Fig. 5 (a) for the snapshot at the instant $t_1 = 40$ ms, right before the time modulation. After the sudden change at time $t = t_1$, the wave propagation direction $\mathbf{k}$ and displacement vector $\mathbf{u}(t_1)$ are preserved in the anisotropic medium as shown in Fig. 5 (b). After the time t_1, the particle motion becomes dominated by the Lissajous polarization [45], which arises as a result of the superposition of qP and qS eigenmodes with different frequencies. At the end time $t_2 = 41.861$ ms, the displacement vector $\mathbf{u}(t_2)$ becomes vertical to $\mathbf{u}(t_1)$. According to the continuity condition, the displacement vector $\mathbf{u}(t_2)$ is preserved when the medium is changed back to the isotropic one at time $t = t_2$. Now, the particle motion follows the transverse polarization because $\mathbf{u}(t_2)$ is perpendicular to the wave propagation direction $\mathbf{k}$, as shown in Fig. 5(c).

According to above analyses, the different phase accumulation in the direction of the two eigenvectors in the orthotropic layer is a critical factor to complete mode conversion. It can be derived from Eqs. (21) and (22) that the qP and qS eigenmodes undergo phase shifts of 2π and π, respectively. This results in the Lissajous polarization which induces the rotation of the displacement vector in the time period from t_1 to t_2. The condition (23) warrants that the rotation angle of the displacement vector is $\pi/2$. This leads to the perpendicular relation between $\mathbf{u}(t_1)$ and $\mathbf{u}(t_2)$, which can be considered as the manifestation of the complete mode conversion

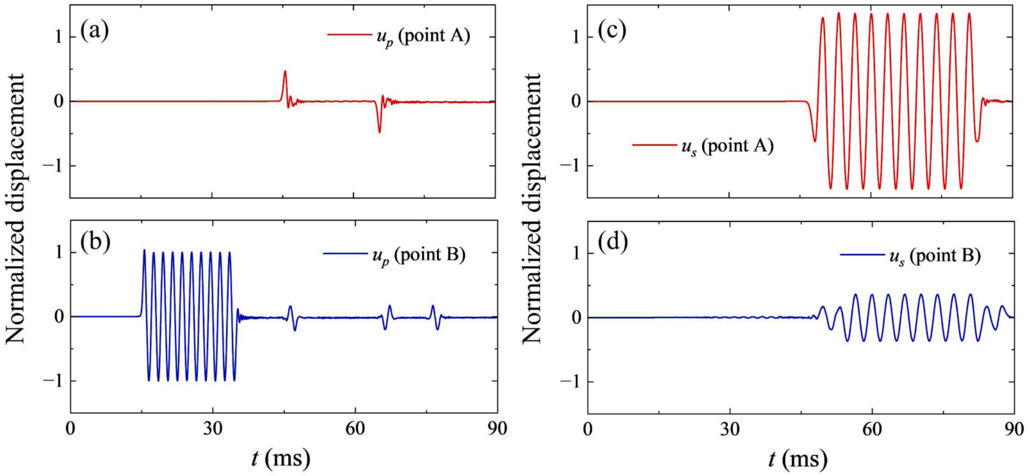

Fig. 7. The time-domain results of (a,b) P-wave and (c,d) S-wave components of displacement fields at measurement points A and B.

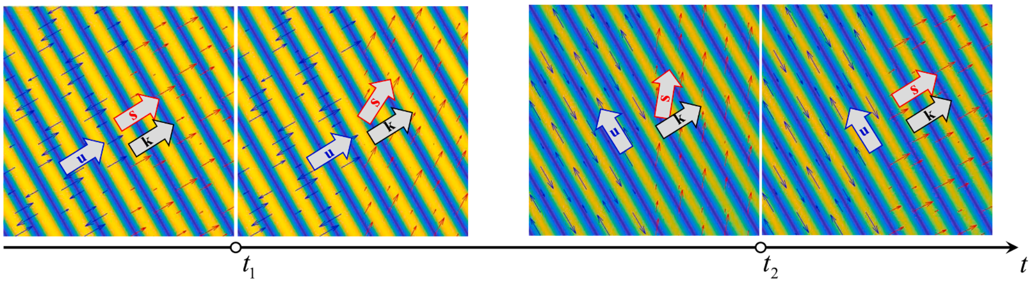

Fig. 8. The displacement fields at two temporal interfaces $t_1 = 40$ ms and $t_2 = 41.861$ ms. Red, blue and black arrows represent Poynting vectors **S**, displacement vectors **u** and wavevectors **k**, respectively.

condition (21)-(23). Based on above analyses, it is readily understood that the complete mode conversion cannot occur when the orthotropic medium is replaced with an isotropic one, because in this case, the polarization in the middle layer will be of the linear profile rather than Lissajous one, as similar to the results of electromagnetic waves [50].

Time-domain simulation analyses

In this section, we numerically validate the TTMM results by Finite-Difference-Time-Domain (FDTD) simulations with algorithms as provided in AppendixB. The simulation domain is a square area of side length $100a$, where a is the wavelength of incident frequency, as shown in Fig. 6 (b). The excitation is chosen as the N-cycle harmonic line source modulated with the Gaussian distribution, where the displacement component along the line normal $\mathbf{n}$ is set as

$$u_n(\mathbf{x},t) = A_0 e^{-\frac{|\mathbf{x}-\mathbf{x}_0|^2}{2\sigma^2}} H(N/f_s - t)\sin(2\pi f_s t)$$

where $\mathbf{x}_0$ refers to the line center, σ is $0.27L$ with the line length $L = 35\mathrm{a}$, f_s is the source frequency, $H(z)$ is the Heaviside step function, and we set $N = 10$. FDTD simulation results have been depicted in Fig. 4, showing the excellent agreement with theoretical results.

To understand the process of polarization conversion, the snapshots of the curl and divergence components of displacement field at 40 ms ($t = t_1$), 40.93 ms ($t_1 < t < t_2$) and 60 ms ($t > t_2$) are provided in Fig. 6 (b-f), respectively. The incident longitudinal wave (Fig. 6 (b)) undergoes the mode conversion in the orthotropic medium as shown in Fig. 6 (c,d). After the sudden change at $t_2 = 41.86$ ms, the divergence component in Fig. 6 (f) vanishes, signifying that the incident wave has been converted into a pure S wave. Examples of perfect S-to-P and partial P-to-S mode conversion are given in AppendixC to provide a comprehensive understanding of underlying physics of temporal interface.

Fig. 7 shows the time-domain responses of u_p and u_s normalized by the amplitude of incident wave at two points A and B, as sketched in Fig. 6 (a,b), which are located 7.5a and 22.5a away from the line source to record transmitted and reflected wave signals,

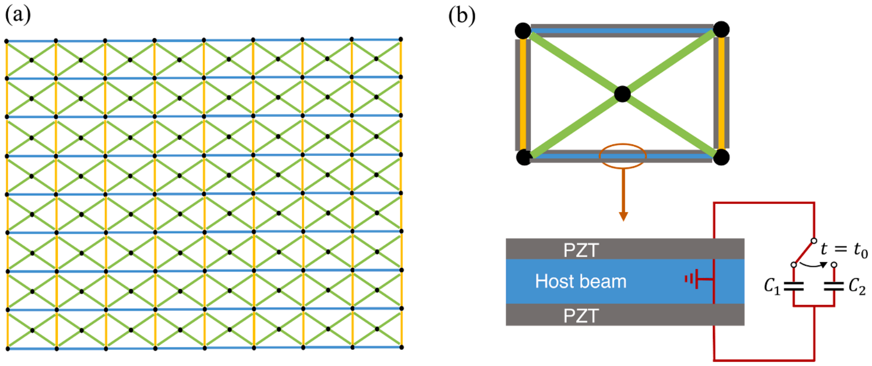

Fig. 9. (a) Schematic of a periodic square lattice structure for physical realization of medium systems with temporal interfaces, and (b) its unit cell consisting of piezoelectric composite structures shunted with the external circuit.

respectively. Notice that $u_p = u_x\cos\alpha + u_y\sin\alpha$ and $u_s = u_x\sin\alpha + u_y\cos\alpha$. It can be found that the transmitted and reflected P-waves are extremely weak after the temporal interface, and the transmissivity and reflectivity of S-waves are 136.6% and 36.6%, in agreement with the theoretical predictions shown in Fig. 4. Small residual P-wave components appearing at the beginning and end of the converted wave are due to the finite duration of the excitation signal used in the computation. In addition, it can be observed that the time oscillation period of transmitted and reflected S-waves are same, but has increased by a factor of $\sqrt{3}$ compared with that of the incident P-wave, confirming the frequency conversion as indicated by the temporal Snell's law.

It is also interesting to examine the energy flux of the system during the time modulation. Fig. 8 shows the displacement field distribution at different instants calculated by the FDTD method. Based on displacement fields, the Poynting vector $\mathbf{S} = -\boldsymbol{\sigma}\cdot\mathbf{v}$ can be calculated. The angle of direction is $\theta_z = \tan^{-1}(S_y/S_x)$ where $\mathbf{S} = \left[S_x, S_y\right]^{\mathrm{T}}$, as marked by red arrows. In the initial isotropic medium ($t < t_1$), θ_s is calculated as 30° and is parallel with the wavevector ($\mathbf{k}$) direction. Across the temporal interface $t = t_1$, the velocity field $\mathbf{v}$ remains continuous while the stress tensor undergoes an instantaneous change, resulting in a sudden change of the energy flow direction from $\theta_s|_{t=t_1^-} = 30^\circ$ to $\theta_s|_{t=t_1^+} = 61^\circ$ This phenomenon has been utilized in electromagnetic wave systems to redirect a wavepacket to a specific location via temporal interfaces [49]. In the orthotropic layer ($t_1 < t < t_2$), the direction of $\mathbf{S}$ varies continuously with time and reaches $\theta_s|_{t=t_2^-} = 81^\circ$ right before $t = t_2$. Across this temporal interface, a sudden change of the energy flow direction occurs leading to $\theta_s|_{t=t_2^+} = 30^\circ$ This process is accompanied by a rotation of displacement field from 30° to 120° , as represented by the blue arrows in Fig. 8. The complete mode conversion across the anisotropic temporal interface is accompanied by a deflection of the energy flux vector, fundamentally attributed to its frequency-shifting characteristics.

Physical realization of medium systems with temporal interfaces

Medium systems with temporal interfaces can be physically realized by two-dimensional lattice structures involving piezoelectric materials and shunting circuits, as sketched in Fig. 9. The unit cell consists of piezoelectric composite beams arranged in a square lattice, and a pair of crossing beams are embedded within the cell. The piezoelectric composite beam is a sandwiched structure composed of two piezoelectric patches attached on both sides of a host beam. Piezoelectric materials are shunted with the external circuit involving the capacitance, which has a great effect on elastic modulus of piezoelectric layers [55]. Therefore, effective stiffness of piezoelectric composite beams can be engineered by tuning geometric and material parameters of building elements and circuit parameters. By designing piezoelectric composite beams in two perpendicular directions, overall elastic properties of lattice structures can be manipulated to fulfill either isotropic or anisotropic elasticity as required in the medium system. In addition, the modulus property can be dynamically modulated by temporally changing the circuit elements. For example, the temporal interface at time $t = t_0$ can be realized by switching the capacitance of value C_1 to a different one C_2. This could be readily implemented by using a circuit control system. Notice that the capacitance can also take negative values realized by using negative impedance circuits, thereby enabling a wide range of stiffness modulation. The structured materials presented in Fig. 9 are designed based on realistic materials, and can act as a suitable candidate for physical realization of medium systems with temporal interfaces.

Conclusions

In this work, the concept of temporal interface appearing as the temporal analog of spatial discontinuity is explored in elastic solids. At temporal interfaces, the momentum and displacement are conserved, while the frequency conversion occurs due to the breaking of temporal translation symmetry. A general temporal transfer matrix method is developed to model elastic wave propagation in temporally layered structures with arbitrary orthotropic material parameters and incident angles. Complete mode conversion from P to S wave mode is showcased through an isotropic-anisotropic-isotropic temporal slab, and is validated by the FDTD method. Due to the frequency-switching nature of the isotropic-anisotropic temporal interface, elastic waves exhibit a Lissajous polarization pattern and a change of Poynting vector in the middle layer. We also dislcose that different phase accumulation of two eigenmodes supported by the orthotropic material is key to the realization of perfect mode conversion. Our findings reveal the interaction mechanism between elastic waves and time-varying materials, and provide both analytical and numerical tools for analyzing elastic waves in temporal solids.

CRediT authorship contribution statement

Cong Chen: Writing – review & editing, Writing – original draft, Visualization, Methodology, Investigation, Data curation, Conceptualization. **Zhanyu Li:** Writing – review & editing, Validation, Methodology. **Xiaoming Zhou:** Writing – review & editing, Visualization, Conceptualization. **Gengkai Hu:** Writing – review & editing, Project administration, Conceptualization.

Declaration of competing interest

The authors declare that they have no known competing financial interests or personal relationships that could have appeared to influence the work reported in this paper.

Acknowledgements

This work was supported by the National Key R&D Program of China (2024YFB3408700 and 2024YFB3408702), and National Natural Science Foundation of China (Grants No. 11632003, No. 11972083, No. 11991030, No. 12225203, No. 12532006). The authors thank Xu Jingwei, Yi Kaijun and Sun Dingxin for helpful discussions.

Appendix A. TTMM for time-varying anisotropic mass density tensor

In Section 2, TTMM for time-varying elasticity tensor is given. In this appendix, we will consider the case that the mass density undergoes an abrupt change at temporal interfaces. Based on the continuity of displacement and particle momentum, the relationship between the wave amplitudes in the n^{th} layer and the $n+1^{th}$ layer can be written as

$$\begin{gathered}
\sum_{m=1}^{4} A_m^n \mathbf{u}_m^n \widehat{\mathbf{x}} e^{i\omega_m^n \tau_n} = \sum_{m=1}^{4} A_m^{n+1} \mathbf{u}_m^{n+1} \widehat{\mathbf{x}} \\
\sum_{m=1}^{4} A_m^n \mathbf{u}_m^n \widehat{\mathbf{y}} e^{i\omega_m^n \tau_n} = \sum_{m=1}^{4} A_m^{n+1} \mathbf{u}_m^{n+1} \widehat{\mathbf{y}} \\
\rho_{11}^n \sum_{m=1}^{4} A_m^n \mathbf{v}_m^n \widehat{\mathbf{x}} e^{i\omega_m^n \tau_n} + \rho_{12}^n \sum_{m=1}^{4} A_m^n \mathbf{v}_m^n \widehat{\mathbf{y}} e^{i\omega_m^n \tau_n} = \rho_{11}^{n+1} \sum_{m=1}^{4} A_m^{n+1} \mathbf{v}_m^{n+1} \widehat{\mathbf{x}} + \rho_{12}^{n+1} \sum_{m=1}^{4} A_m^n \mathbf{v}_m^n \widehat{\mathbf{y}} \\
\rho_{12}^n \sum_{m=1}^{4} A_m^n \mathbf{v}_m^n \widehat{\mathbf{x}} e^{i\omega_m^n \tau_n} + \rho_{22}^n \sum_{m=1}^{4} A_m^n \mathbf{v}_m^n \widehat{\mathbf{y}} e^{i\omega_m^n \tau_n} = \rho_{12}^{n+1} \sum_{m=1}^{4} A_m^{n+1} \mathbf{v}_m^{n+1} \widehat{\mathbf{x}} + \rho_{22}^{(n+1)} \sum_{m=1}^{4} A_m^n \mathbf{v}_m^n \widehat{\mathbf{y}}
\end{gathered} \tag{A.1}$$

where $\rho_{11}^n, \rho_{12}^n, \rho_{22}^n$ are the components of anisotropic mass density tensor $\boldsymbol{\rho}^n$. The above expressions can be rewritten as

$$N_n D_n P_n \begin{pmatrix} A_1^n \\ A_2^n \\ A_3^n \\ A_4^n \end{pmatrix} = N_{n+1} D_{n+1} \begin{pmatrix} A_1^{n+1} \\ A_2^{n+1} \\ A_3^{n+1} \\ A_4^{n+1} \end{pmatrix} \tag{A.2}$$

Compared with Eq. (6), there appears an additional matrix N_n with the following form

$$N_n = \begin{pmatrix} 1 & 0 & 0 & 0 \\ 0 & 1 & 0 & 0 \\ 0 & 0 & \rho_{11}^n & \rho_{12}^n \\ 0 & 0 & \rho_{12}^n & \rho_{22}^n \end{pmatrix} \tag{A.3}$$

When the density is constant and isotropic, the matrix N_n reduces to

$$N_n = \begin{pmatrix} 1 & & & \\ & 1 & & \\ & & \rho_0 & \\ & & & \rho_0 \end{pmatrix}. \tag{A.4}$$

Appendix B. FDTD simulation algorithms

The second-order partial derivatives of field $\mathbf{u}(x,y,t) = u(x,y,t)\widehat{\mathbf{x}} + v(x,y,t)\widehat{\mathbf{y}}$ can be approximated as the following expressions by Taylor expansion

$$\begin{aligned} \frac{\partial^2 u}{\partial t^2} &= \frac{u_{i,j}^{n+1} - 2u_{i,j}^{n} + u_{i,j}^{n-1}}{\tau^2} \\ \frac{\partial^2 u}{\partial x^2} &= \frac{u_{i+1,j}^{n} - 2u_{i,j}^{n} + u_{i-1,j}^{n}}{h^2} \\ \frac{\partial^2 v}{\partial x^2} &= \frac{v_{i+1,j}^{n} - 2v_{i,j}^{n} + v_{i-1,j}^{n}}{h^2} \\ \frac{\partial^2 u_y}{\partial x \partial y} &= \frac{u_{i+1,j+1}^{n} + u_{i-1,j-1}^{n} - u_{i-1,j+1}^{n} - u_{i+1,j-1}^{n}}{4h^2} \end{aligned} \tag{B.1}$$

where i and j are the spatial indices representing discretized coordinates x_i and y_j, and n is the temporal index. The spatial and temporal intervals are h and τrespectively. u and v represent the displacements in x and y directions, respectively. By substituting above expressions into Eq. (1), the following recurrence relations can be obtained

$$\begin{aligned} u_{i,j}^{n+1} = 2u_{i,j}^{n} - u_{i,j}^{n-1} + \frac{\tau^2}{\rho}\Bigg(C_{11}\left(\frac{u_{i+1,j}^{n} - 2u_{i,j}^{n} + u_{i-1,j}^{n}}{h^2}\right) + C_{12}\left(\frac{v_{i+1,j+1}^{n} - v_{i+1,j-1}^{n} - v_{i-1,j+1}^{n} + v_{i-1,j-1}^{n}}{4h^2}\right) \\ + C_{66}\left(\frac{u_{i,j+1}^{n} - 2u_{i,j}^{n} + u_{i,j-1}^{n}}{h^2} + \frac{v_{i+1,j+1}^{n} - v_{i+1,j-1}^{n} - v_{i-1,j+1}^{n} + v_{i-1,j-1}^{n}}{4h^2}\right)\Bigg) \\ v_{i,j}^{n+1} = 2v_{i,j}^{n} - v_{i,j}^{n-1} + \frac{\tau^2}{\rho}\Bigg(C_{22}\left(\frac{v_{i,j+1}^{n} - 2v_{i,j}^{n} + v_{i,j-1}^{n}}{h^2}\right) + C_{12}\left(\frac{u_{i+1,j+1}^{n} - u_{i+1,j-1}^{n} - u_{i-1,j+1}^{n} + u_{i-1,j-1}^{n}}{4h^2}\right) \\ + C_{66}\left(\frac{v_{i+1,j}^{n} - 2v_{i,j}^{n} + v_{i-1,j}^{n}}{h^2} + \frac{u_{i+1,j+1}^{n} - u_{i+1,j-1}^{n} - u_{i-1,j+1}^{n} + u_{i-1,j-1}^{n}}{4h^2}\right)\Bigg) \end{aligned} \tag{B.2}$$

The time step τ needs to be sufficiently small to satisfy the Courant condition

$$\tau \leq \frac{h}{\sqrt{2}c} \tag{B.3}$$

In the FDTD simulations, the time and space steps are chosen to be τ=0.01ms and $h = 0.1$a, which satisfy the Courant condition.

Appendix C. Analyses of S-to-P and partial P-to-S mode conversion

Two additional case studies, i.e. S-to-P conversion and partial P to S conversion, are discussed here to give a full picture of the underlying physics of temporal interface.

S-to-P mode conversion

Eqs. (21)-(23) provide a general condition that can not only be used for creating P-to-S mode conversion but also for S-to-P one. To demonstrate the latter case, consider a plane shear wave with the incident angle $\alpha = \pi/6$. The initial and end layers are same to those used in the P-to-S mode conversion case, and $C_{66} = 1$ GPa and $C_{12} = 0.5$ GPa are set for the middle layer. According to Eqs. (21)-(23), system parameters for complete conversion from S to P modes are given by $C_{11} = 1.053$ GPa, $C_{22} = 10.160$ GPa, and Δt=1.04 ms. FDTD calculations based on the simulation model of Fig. 6(a) are conducted to verify the theoretical prediction. Fig. C.1 shows the FDTD results of the curl and divergence components of displacement fields at 40 ms ($t < t_1$), 40.52 ms ($t_1 < t < t_2$) and 60 ms ($t > t_2$). It is clearly seen in Fig. C.1 (c) that the curl component of displacements vanishes, confirming the complete mode conversion from S to P waves.

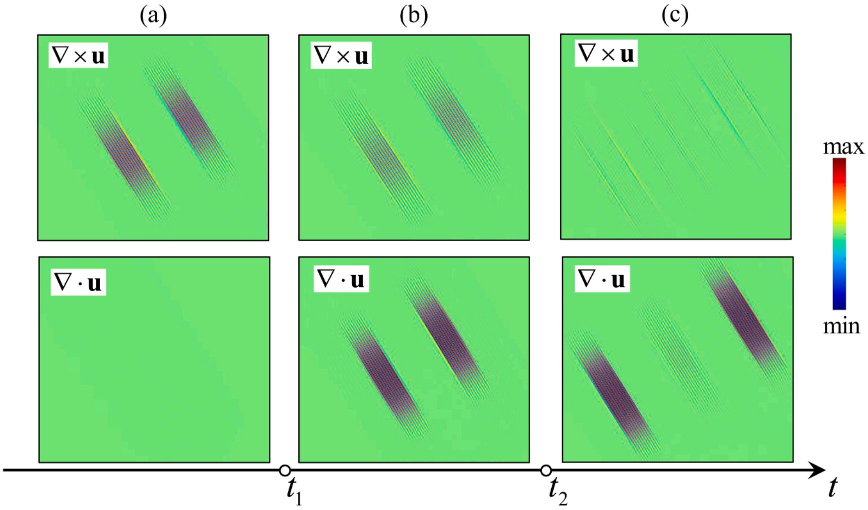

Fig. C.1. FDTD results of wave propagation in the isotropic-anisotropic-isotropic temporal slab: the curl and divergence components of displacement fields at (a) 40 ms, (b) 40.52 ms, and (c) 60 ms, respectively.

Partial P-to-S mode conversion

Complete mode conversion cannot be attained when system parameters deviate from theoretical conditions given by Eqs. (21)-(23). To illustrate this behavior, the time interval Δt is changed to 0.93 ms for the example of P-to-S conversion discussed in Sec. 4.1 while other system parameters are kept unaltered. Fig. C.2 shows the FDTD results of the divergence and curl components of displacement fields at 40 ms ($t < t_1$), 40.75 ms ($t_1 < t < t_2$) and 60 ms ($t > t_2$). Both P and S wave modes can be observed in the end layer at $t > t_2$ as shown in Fig. C.2(c). This is because, unlike in the case of Fig.5 (b), the phase accumulations of qP and qS waves over $\Delta t = 0.93$ ms are π and $\pi/2$, respectively. This results in that the displacement vectors $\mathbf{u}(t_2)$ and $\mathbf{u}(t_1)$ are neither parallel nor perpendicular, leading to the partial mode conversion from P to S waves.

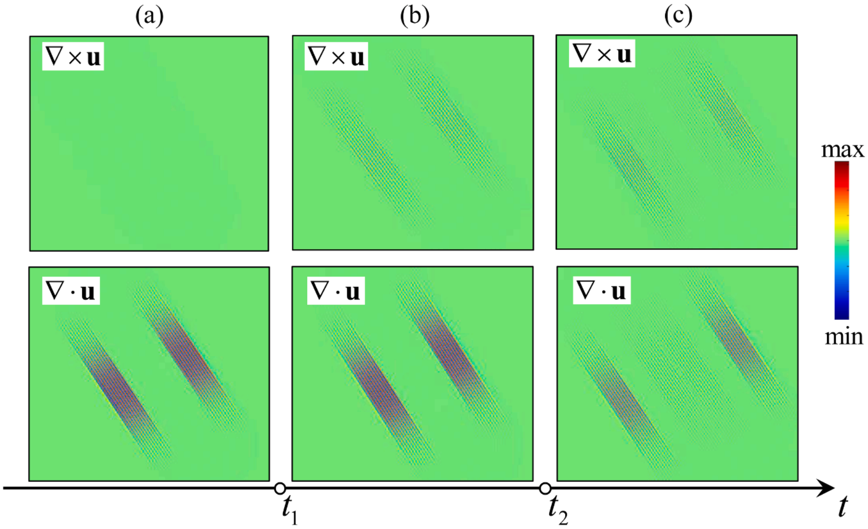

Fig. C.2. FDTD results of wave propagation in the isotropic-anisotropic-isotropic temporal slab: the curl and divergence components of displacement fields at (a) 40 ms, (b) 40.75 ms, and (c) 60 ms, respectively.

Data availability

Data will be made available on request.

References

[1] B.A. Auld, Acoustic fields and waves in solids, Рипол Классик, 1973.
[2] D.N. Alleyne, P. Cawley, The interaction of Lamb waves with defects, IEEE Trans. Ultrason. Ferroelectr. Freq. Control 39 (1992) 381–397.
[3] J.L. Rose, Ultrasonic guided waves in Solid Media, in, 2014.
[4] Y. Okabe, K. Fujibayashi, M. Shimazaki, H. Soejima, T. Ogisu, Delamination detection in composite laminates using dispersion change based on mode conversion of Lamb waves, Smart Mater. Struct. 19 (2010) 115013.
[5] B.F. Kennedy, P. Wijesinghe, D.D. Sampson, The emergence of optical elastography in biomedicine, Nat. Photonics 11 (2017) 215–221.
[6] Y. Tufail, A. Yoshihiro, S. Pati, M.M. Li, W.J. Tyler, Ultrasonic neuromodulation by brain stimulation with transcranial ultrasound, Nat. Protoc. 6 (2011) 1453–1470.
[7] R. Zhu, X.N. Liu, G.K. Hu, C.T. Sun, G.L. Huang, Negative refraction of elastic waves at the deep-subwavelength scale in a single-phase metamaterial, Nat. Commun. 5 (2014) 5510.
[8] Y. Wei, G. Hu, Wave characteristics of extremal elastic materials, Extreme Mech. Lett. (2022) 55.
[9] F. Liu, Z. Liu, Elastic waves scattering without conversion in metamaterials with simultaneous zero indices for longitudinal and transverse waves, Phys. Rev. Lett. 115 (2015) 175502.
[10] H.K. Zhang, Y. Chen, X.N. Liu, G.K. Hu, An asymmetric elastic metamaterial model for elastic wave cloaking, J. Mech. Phys. Solids 135 (2020).
[11] Y. Wu, Y. Lai, Z.-Q. Zhang, Elastic metamaterials with simultaneously negative effective shear modulus and mass density, Phys. Rev. Lett. 107 (2011) 105506.
[12] J.M. Kweun, H.J. Lee, J.H. Oh, H.M. Seung, Y.Y. Kim, Transmodal Fabry-Pérot resonance: theory and realization with elastic metamaterials, Phys. Rev. Lett. 118 (2017).
[13] X. Yang, J.M. Kweun, Y.Y. Kim, Theory for perfect transmodal Fabry-perot interferometer, Sci. Rep. 8 (2018) 69.
[14] X. Yang, Y.Y. Kim, Asymptotic theory of bimodal quarter-wave impedance matching for full mode-converting transmission, Phys. Rev. B 98 (2018) 144110.
[15] X. Yang, M. Kweun, Y.Y. Kim, Monolayer metamaterial for full mode-converting transmission of elastic waves, Appl. Phys. Lett. (2019) 115.
[16] A.A. Oliner, A. Hessel, Wave propagation in a medium with a progressive sinusoidal disturbance, IRE Trans. Microw. Theory Tech. 9 (1961) 337–343.
[17] E.S. Cassedy, A.A. Oliner, Dispersion relations in time-space periodic media: part I—Stable interactions, Proc. IEEE 51 (1963) 1342–1359.
[18] D.L. Sounas, A. Alù, Non-reciprocal photonics based on time modulation, Nat. Photonics 11 (2017) 774–783.
[19] E.S. Cassedy, Waves guided by a boundary with time—Space periodic modulation, Proc. Inst. Electr. Eng. 112 (1965) 269–279.
[20] V. Bacot, M. Labousse, A. Eddi, M. Fink, E. Fort, Time reversal and holography with spacetime transformations, Nat. Phys. 12 (2016) 972–977.
[21] V. Krylov, S.V. Sorokin, Dynamics of elastic beams with controlled distributed stiffness parameters, Smart Mater. Struct. 6 (1997) 573.
[22] K.A. Lurie, S.L. Weekes, Some new advances in the theory of dynamic materials, in: 2003 IEEE International Workshop on Workload Characterization (IEEE Cat. No.03EX775), 2003, pp. 1326–1335, vol.1324.
[23] J. Huang, X. Zhou, A time-varying mass metamaterial for non-reciprocal wave propagation, Int. J. Solids Struct. 164 (2019) 25–36.
[24] X. Zhou, J. Huang, Non-reciprocal metamaterials with simultaneously time-varying stiffness and mass, J. Appl. Mech. 87 (2020).
[25] G. Trainiti, M. Ruzzene, Non-reciprocal elastic wave propagation in spatiotemporal periodic structures, New J. Phys. 18 (2016) 083047.
[26] K. Yi, S. Karkar, M. Collet, One-way energy insulation using time-space modulated structures, J. Sound Vib. 429 (2018) 162–175.
[27] J. Marconi, E. Riva, M. Di Ronco, G. Cazzulani, F. Braghin, M. Ruzzene, Experimental observation of nonreciprocal band gaps in a space-time-modulated beam using a shunted piezoelectric array, Phys. Rev. Appl. 13 (2020) 031001.
[28] M.A. Attarzadeh, J. Callanan, M. Nouh, Experimental observation of nonreciprocal waves in a resonant metamaterial beam, Phys. Rev. Appl. 13 (2020) 021001.
[29] L. Shui, Y. Liu, X. Chen, Snell's law of elastic waves propagation on moving property interface of time-varying materials, Int. J. Solids Struct. 143 (2018) 18–28.
[30] A. Delory, C. Prada, M. Lanoy, A. Eddi, M. Fink, F. Lemoult, Elastic wave packets crossing a space-time interface, Phys. Rev. Lett. 133 (2024) 267201.
[31] G.W. Milton, J.R. Willis, On modifications of Newton's second law and linear continuum elastodynamics, Proc. R. Soc. A: Math. Phys. Eng. Sci. 463 (2007) 855–880.
[32] Y. Chen, X. Li, G. Hu, M.R. Haberman, G. Huang, An active mechanical Willis meta-layer with asymmetric polarizabilities, Nat. Commun. (2020) 11.
[33] H. Nassar, X.C. Xu, A.N. Norris, G.L. Huang, Modulated phononic crystals: non-reciprocal wave propagation and Willis materials, J. Mech. Phys. Solids 101 (2017) 10–29.
[34] D.W. Wright, R.S.C. Cobbold, Acoustic wave transmission in time-varying phononic crystals, Smart Mater. Struct. 18 (2009) 015008.
[35] K.A. Lurie, V.V. Yakovlev, Energy accumulation in waves propagating in space- and time-varying transmission lines, IEEE Antennas Wirel. Propag. Lett. 15 (2016) 1681–1684.
[36] G.W. Milton, O. Mattei, Field patterns: a new mathematical object, Proc. Math. Phys. Eng. Sci. 473 (2017) 20160819.
[37] O. Mattei, G.W. Milton, Field patterns without blow up, New J. Phys. 19 (2017).
[38] M.B. Zanjani, A.R. Davoyan, N. Engheta, J.R. Lukes, NEMS with broken T symmetry: graphene based unidirectional acoustic transmission lines, Sci. Rep. 5 (2015) 9926.
[39] J. Santini, X. Pu, A. Palermo, F. Braghin, E. Riva, Controlling surface acoustic waves (SAWs) via temporally graded metasurfaces, 2024.
[40] J. Santini, E. Riva, Elastic temporal waveguiding, New J. Phys. 25 (2023) 013031.
[41] N. Swinteck, S. Matsuo, K. Runge, J.O. Vasseur, P. Lucas, P.A. Deymier, Bulk elastic waves with unidirectional backscattering-immune topological states in a time-dependent superlattice, J. Appl. Phys. (2015) 118.
[42] C. Cho, X. Wen, N. Park, J. Li, Digitally virtualized atoms for acoustic metamaterials, Nat. Commun. (2020) 11.
[43] E. Galiffi, R. Tirole, S. Yin, H. Li, S. Vezzoli, P.A. Huidobro, M.G. Silveirinha, R. Sapienza, A. Alú, J.B. Pendry, Photonics of time-varying media, Adv. Photonics 4 (2021), 014002 - 014002.
[44] C. Caloz, Z.-L. Deck-Léger, Spacetime Metamaterials—Part I: general concepts, IEEE Trans. Antennas Propag. 68 (2020) 1569–1582.
[45] A. Akbarzadeh, N. Chamanara, C. Caloz, Inverse prism based on temporal discontinuity and spatial dispersion, Opt. Lett. 43 (2018) 3297–3300.
[46] V. Pacheco-Peña, N. Engheta, Antireflection temporal coatings, Optica 7 (2020) 323–331.
[47] J. Zhang, W.R. Donaldson, G.P. Agrawal, Time-domain Fabry–Perot resonators formed inside a dispersive medium, J. Opt. Soc. Am. B 38 (2021) 2376–2382.
[48] J. Xu, W. Mai, D.H. Werner, Complete polarization conversion using anisotropic temporal slabs, Opt. Lett. (2021) 46.
[49] V. Pacheco-Peña, N. Engheta, Temporal aiming, light: science and applications, 9 (2020) 129. https://doi.org/10.1038/s41377-020-00360-1.
[50] V. Pacheco-Peña, N. Engheta, Temporal equivalent of the Brewster angle, Phys. Rev. B 104 (2021) 214308.
[51] H. Moussa, G. Xu, S. Yin, E. Galiffi, Y. Ra'di, A. Alù, Observation of temporal reflection and broadband frequency translation at photonic time interfaces, Nat. Phys. 19 (2023) 863–868.
[52] B.L. Kim, C. Chong, C. Daraio, Temporal refraction in an acoustic phononic lattice, Phys. Rev. Lett. (2024) 133.
[53] S. Wang, N. Shao, H. Chen, J. Chen, H. Qian, Q. Wu, H. Duan, A. Alu, G. Huang, Temporal refraction and reflection in modulated mechanical metabeams: theory and physical observation, arXiv preprint arXiv:2501.09989, (2025).
[54] A. Ortega-Gomez, M. Lobet, J.E. Vázquez-Lozano, I. Liberal, Tutorial on the conservation of momentum in photonic time-varying media [Invited], Opt. Mater. Express 13 (2023) 1598.
[55] K. Yi, M. Collet, Broadening low-frequency bandgaps in locally resonant piezoelectric metamaterials by negative capacitance, J. Sound Vib. (2021) 493.